

Article

The Influence of Wettability Effect and Adsorption Thickness on Nanoconfined Methane Phase Behavior: Vapor-Liquid Co-Existence Curves and Phase Diagrams

Guodai Wu^{1,2,3}, Chunlin Zeng^{1,2}, Lijun Cheng^{1,2}, Jinhua Luan^{1,2,3}, Ruigang Zhang^{1,2,3}, Ziwei Chen^{1,2}, Yu Pang⁴ and Zheng Sun^{3,*}

- ¹ National and Local Joint Engineering Research Center of Shale Gas Exploration and Development, Chongqing Institute of Geology and Mineral Resources, Chongqing 401120, China
- ² Key Laboratory of Shale Gas Exploration, Ministry of Natural Resources, Chongqing Institute of Geology and Mineral Resources, Chongqing 401120, China
- ³ State Key Laboratory of Coal Resources and Safe Mining, China University of Mining and Technology, Xuzhou 221116, China
- ⁴ College of Energy Resources, Chengdu University of Technology, Chengdu 610059, China
- * Correspondence: sunzheng@cumt.edu.cn; Tel.: +86-185-0061-0758; Fax: +86-108-9734-951

Abstract: Research interest in the behavior of methane inside nanopores has been growing, driven by the substantial geological reserves of shale gas and coalbed methane. The phase diagram of methane in nanopores differs significantly from its bulk state, influencing its existing form and pertinent physical properties—such as density and viscosity—at specific pressures and temperatures. Currently, there is a lack of effort to understand the nanoconfinement effect on the methane phase diagram; this is a crucial issue that needs urgent attention before delving into other aspects of nanoconfined methane behavior. In this study, we establish a fully coupled model to predict the methane phase diagram across various scales. The model is based on vapor-liquid fugacity equilibrium, considering the shift in critical pressure and temperature induced by pore size shrinkage and adsorption-phase thickness. Notably, our proposed model incorporates the often-overlooked factor of capillary pressure, which is greatly amplified by nanoscale pore size and the presence of the adsorption phase. Additionally, we investigated the impact of surface wettability, correlated to capillary pressure and the shift in critical properties, on the methane phase diagram. Our results indicate that (a) as pore size decreases, the methane phase diagram becomes more vertical, suggesting a transition from a gaseous to a liquid state for some methane molecules, which is contrary to the conventional phase diagram; (b) enhancing surface wettability results in a more vertical phase diagram, with the minimum temperature corresponding to 0 MPa pressure on the phase diagram, increasing by as much as 87.3%; (c) the influence of capillary pressure on the phase diagram is more pronounced under strong wettability conditions compared to weak wettability, and the impact from the shift in critical properties can be neglected when the pore size exceeds 50 nm.

Keywords: methane phase behavior; nanopores; wettability; adsorption; vapor-liquid co-existence



Citation: Wu, G.; Zeng, C.; Cheng, L.; Luan, J.; Zhang, R.; Chen, Z.; Pang, Y.; Sun, Z. The Influence of Wettability Effect and Adsorption Thickness on Nanoconfined Methane Phase Behavior: Vapor-Liquid Co-Existence Curves and Phase Diagrams. *Processes* **2024**, *12*, 215. <https://doi.org/10.3390/pr12010215>

Academic Editor: Juan Carlos Moreno-Piraján

Received: 2 January 2024

Revised: 12 January 2024

Accepted: 16 January 2024

Published: 18 January 2024



Copyright: © 2024 by the authors. Licensee MDPI, Basel, Switzerland. This article is an open access article distributed under the terms and conditions of the Creative Commons Attribution (CC BY) license (<https://creativecommons.org/licenses/by/4.0/>).

1. Introduction

Adequate energy supply forms the foundation of economic development and social stability. Methane, the primary component of natural gas, has been a dominant force in the commonly consumed fossil energy over the past decades [1,2]. Massive engineering projects across the world have tried to exploit methane resources from natural gas reservoirs as much as possible. The methane reserve in conventional gas reservoirs, characterized by relatively large pore sizes ranging from several microns to thousands of microns, is inadequate to meet the current growing energy demand [3,4]. As a result, the significant geological methane reserves in unconventional gas reservoirs, such as shale gas, tight gas,

and coalbed methane [5,6], have garnered attention. The development of unconventional gas reservoirs presents a new pathway for obtaining methane. It is worth noting that the typical pore size in unconventional gas reservoirs falls within the nanoscale [7,8], comparable to the molecular diameter of methane, which is 0.38 nm. This results in methane behavior in nanopores being significantly different from bulk methane [9–12]. Furthermore, the classic theoretical framework designed for bulk methane is inadequate for characterizing the physical properties of nanoconfined methane, including existence phase, density, viscosity, and so on. As a result, a significant amount of research effort has been dedicated to shedding light on methane behavior under nanoconfinement.

The focus of most research lies in understanding nanoconfined methane transport and adsorption capacity, representing gas production and geological reserves, respectively [13,14]. The traditional Darcy function, rooted in the Navier–Stokes (NS) equation, falls short of predicting nanoconfined methane flow capacity. Discrepancies between realistic flow capacity in nanopores and that evaluated by the NS equation can be substantial, reaching several magnitudes [15,16]. This discrepancy arises from boundary slip in nanopores, where methane molecules near the pore wall exhibit mobility, unlike in macro-pores [17,18]. In order to bridge this knowledge gap, various boundary conditions, such as first-order and second-order conditions [19,20], are proposed to modify the NS equation, considering the boundary slip mechanism. Some scholars argue that intermolecular collisions dominate gas flow in macropores [21,22], while molecule-wall collisions dominate nanoconfined gas flow. A model for nanoconfined gas flow was established, superimposing continuum flow capacity and free-molecule diffusion [23,24]. This model covers gas flow mechanisms over different scales, reverting to the NS equation when the Knudsen number is less than 0.001 and gradually transitioning to free-molecule diffusion when the Knudsen number exceeds 10. Despite its theoretical background, the model aligns well with existing works. While some research provides empirical formulas based on experimental data using advanced data acquisition methods [25,26], their applicability is limited, as the current experimental pore sizes are challenging to reach at the nanoscale. Recent updates in nanoconfined gas flow consider surface roughness, real gas effects, pore geometry, etc. Regarding nanoconfined gas adsorption, approaches such as molecular dynamics (MDs) and the lattice Boltzmann method, along with experiments, explore adsorption from a microscopic viewpoint [27,28]. MDs, particularly, is used to calculate the velocity and relative position of each particle in a simulation box containing tens of thousands of particles [29,30]. It is valuable for studying competition adsorption on surfaces with specific compositions, advancing development in nanopore-rich unconventional gas reservoirs [31,32]. The lattice Boltzmann method is another theoretical calculation approach, and the laboratory experiments directly measure gas adsorption capacity in an in-situ core [33,34]. After this brief review of nanoconfined gas transport and adsorption, it is crucial to highlight that resolving the phase behavior in nanopores is the initial challenge before exploring transport and adsorption issues. Methane phase behavior, indicating the existence phase at specific pressure and temperature conditions, significantly influences density and viscosity, which are key factors dominating the nanoconfined transport and adsorption capacity. However, knowledge about nanoconfined methane phase behavior is still vague, with limited research on bulk and nanopore conditions. In nanopores, capillary pressure, typically negligible in bulk conditions, must be considered, and the presence of the adsorption phase near the nanopore wall reinforces its impact. Additionally, the shift in critical properties [35,36], including critical pressure and temperature, in nanopores should be incorporated. These factors both distinguish and complicate the understanding of nanoconfined phase behavior compared to bulk behavior.

In this paper, we establish a comprehensive theoretical framework aligned with basic thermodynamics theory to delineate the methane phase envelope in nanopores. This framework incorporates the simultaneous consideration of critical property shifts, adsorption-phase thickness, and capillary pressure. The paper's organization is outlined below. Initially, Section 2 presents the specific differences in methane phase behavior

across various pore scales, illustrating the influences of adsorption-phase thickness and capillary pressure. Subsequently, a theoretical model is developed based on liquid-vapor fugacity equilibrium, with the model's reliability well-verified through nanoconfined phase behavior primarily measured by MDs. Following this, a sensitivity analysis is conducted to reveal the impact of factors, such as pore size, surface wettability, capillary pressure, and the shift of critical properties, on nanoconfined methane phase behavior. Lastly, several conclusions are drawn.

2. Physical Model

Before establishing the model for the nanoconfined methane envelope, it is crucial to understand the fundamental mechanisms that contribute to the abnormal phase behavior in nanopores compared to the macroscale. As illustrated in Figure 1, gas molecules freely distribute inside macropores, where the pore size is thousands of times that of the molecular size. Consequently, the influences exerted by the pore surface can be neglected. Simultaneously, the capillary pressure, representing the difference between vapor phase pressure and liquid phase pressure at vapor-liquid coexistence, can be overlooked, approaching zero as the pore size becomes significantly large [37,38]. In contrast, when the pore size shrinks to the nanoscale and becomes comparable to the molecular size, molecular adsorption resulting from molecule-wall interactions plays a crucial role in influencing gas behavior. Initially, the adsorbed molecules occupy space near the pore surface, further reducing the pore size [39,40]. Meanwhile, the critical properties exhibit a noticeable decline tendency with the reduction in pore size, especially when the pore size falls within the nanoscale. More importantly, capillary pressure experiences a significant increase within nanoscale pore sizes, leading to a substantial variation in the nanoconfined gas envelope. Unfortunately, the magnitude and the specific way these factors, including adsorption-phase thickness, capillary pressure, and shifted critical properties, affect nanoconfined phase behavior remain open questions. This work aims to address and fill this knowledge gap. Unraveling this issue would provide a clear understanding of the gas's existence state at given pressure and temperature conditions. It would also offer reliable estimates of gas density and viscosity, laying a solid foundation for research on gas transport and adsorption in nanopores.

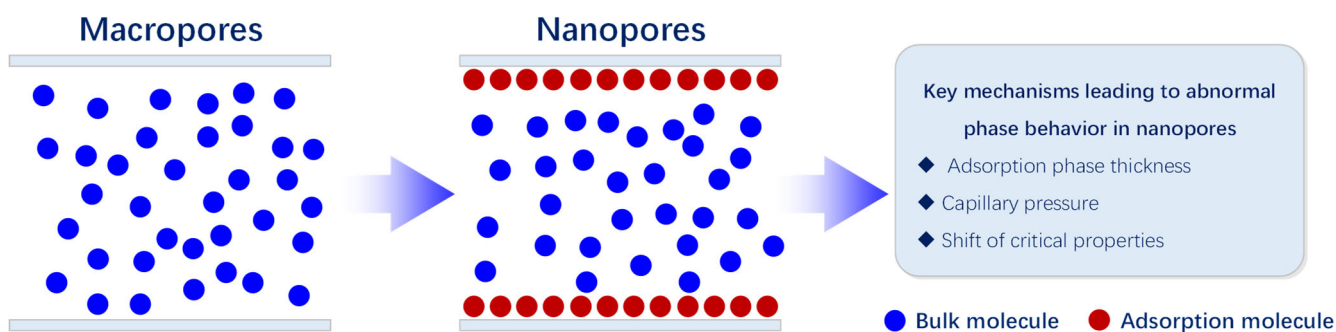


Figure 1. Inherent mechanism resulting in variable phase behavior over pore scales.

Several preconditions, simplifying the procedures for establishing the model, are outlined below. Firstly, the nanopore geometry is assumed to be a circle, and the surface is considered completely smooth. It is assumed that a virtual line exists that distinguishes the adsorption phase from the bulk-like phase in nanopores. The molecular behavior in the bulk-like region follows basic thermodynamics theory. Additionally, the thickness of the adsorption phase is assumed to be consistent regardless of relative positions. Furthermore, it is assumed that molecular adsorption does not influence the wettability effect that the pore surface imposes on bulk-like molecules in nanopores.

3. Model Establishment

While the influence of surface molecules on confined gas molecules in nanopores differs from that in macropores, molecular behavior still adheres to fundamental thermodynamics. Therefore, in this work, the proposed model is developed based on liquid-vapor fugacity equilibrium derived from the modified PR-EOS. This model considers the adsorption-phase thickness and shifted critical properties, as well as capillary pressure.

3.1. Adsorption-Phase Thickness

As illustrated in Figure 1, the adsorption phenomenon takes place in nanopores; its thickness will occupy the space near the pore surface. It should be noted that adsorption molecules are arranged tightly and orderly [41,42], and this is apparently different from the freely distributed bulk-like molecules. As reported, adsorption-phase molecules tend to behave like those in a solid phase, which is hard to describe by using the mentioned PR-EOS. At the same time, the presence of the adsorption phase narrows the effective pore space where bulk-like molecules fill. Zhang et al. (2019) proposed a formula correlating adsorption-phase thickness to pore size [43] and gas molecular molar weight, which is provided below. The correlation suggests the adsorption-phase thickness enlarges with the decline in pore size, which is able to reach agreements with existing MDs and experiments on gas adsorption capacity.

$$H_{ad} = \frac{\alpha}{\ln(m)} + \frac{\beta}{m} \quad (1)$$

$$m = \frac{R}{\sigma} \quad (2)$$

$$\alpha = -8.314 \times 10^{-5} MW^2 + 2.0475 \times 10^{-2} MW + 3.0886 \times 10^{-2} \quad (3)$$

$$\beta = -6.3565 \times 10^{-5} MW^2 + 3.155 \times 10^{-2} MW - 0.58538 \quad (4)$$

where m is the characteristic pore size with the definition as a ratio of pore radius (R) to molecular diameter; the concrete formula is Equation (2), which is dimensionless; σ is molecular gas diameter, which is 0.38 nm since the gas type is methane; MW is the methane molar weight: 16 g/mol.

In accordance with Equations (1) and (2), adsorption-phase thickness (H_{ad}) can be readily obtained, and the effective pore size that equals the original pore radius minus H_{ad} can be obtained as well, which can be utilized in calculating capillary pressure as well as shifts in the critical properties.

3.2. Shift in Critical Properties

Lots of experimental evidence and simulation data from molecular dynamics indicate that the critical pressure and critical temperature of nanoconfined substances would decline to a certain extent, considering that they are key underlying mechanisms for abnormal phase behavior in nanopores. With the motivation of capturing the relationship between the shift in critical properties and nanopore dimension, a great deal of models designed to reproduce the nanoconfined critical properties have been developed. Notably, the majority of the existing models use empirical formulas by fitting experimental data or simulations collected from previous research [44,45], lacking the necessary theoretical background. Meanwhile, some models are derived from the thermodynamic EOS modified by surface-molecule interactions. However, the fatal deficiency these models mainly suffer from is overlooking the wettability effect; in the other words, the outputs yielded from the models fail to characterize the nanoconfined phase behavior by varying surface contact angle. In this regard, the model that is rooted in modified EOS and density function theory (DFT) proposed by Feng et al. (2021) is employed here [46], which considers the impact of pore size shrinkage and wettability effect simultaneously. Particularly, the adsorption-phase thickness reducing the pore size is properly considered in Equations (5) and (6) by updating the correlation for characteristic pore size from m to m_e . In accordance with

the following formulas, a shift in magnitude is related not only to pore size but also to the wettability effect, which would increase as the surface contact angle decreases. The surface-molecule interaction strength intensifies with a stronger wettability effect, indicating more molecules would be affected by surface molecules, which further suggests that nanoconfined molecules behave more differently compared to bulk-like molecules.

$$\frac{T_{cb} - T_c}{T_{cb}} = \frac{\tau}{m_e} \quad (5)$$

$$\frac{P_{cb} - P_c}{P_{cb}} = \frac{\tau}{m_e} \quad (6)$$

$$m_e = \frac{R - H_{ad}}{\sigma} \quad (7)$$

$$\tau = \zeta \times \chi \quad (8)$$

$$\chi = 0.65 \ln\left(\frac{180}{\theta}\right) \quad (9)$$

where T_{cb} and P_{cb} are methane's critical temperature and critical pressure in the bulk condition, respectively; T_c and P_c are nanoconfined critical temperature and critical pressure (considering the shift), respectively; m_e is the effective characteristic pore size, defined as the ratio of effective pore size to molecular diameter, which is dimensionless; τ captures the relative strength between intermolecular interactions and molecule-surface interactions, which is dimensionless; ζ is the constant coefficient, which is 0.56 for cylindrical nanopores; θ is the contact angle, the direct parameter characterizing wettability effect, in $^\circ$.

3.3. Capillary Pressure

In essence, capillary pressure is the pressure difference between vapor-phase pressure and liquid-phase pressure, which is inversely proportional to pore size. As a result, capillary pressure cannot be neglected at the nanoscale, which turns out to be relatively good at dramatically varying vapor-phase density and liquid-phase density [47,48], further affecting phase behavior. Notably, when compared with the conventional formula for capillary pressure, Formula (11) (designed for nanoconfined capillary pressure) takes into account the adsorption-phase thickness. At the same time, the capillary pressure that may change direction as the contact angle changes is presented by Equation (10).

$$P_{nw} = P_w + P_c \quad (10)$$

$$P_c = \frac{2\sigma_c \cos \theta}{r - H_{ad}} \quad (11)$$

where P_w and P_{nw} are the wet phase pressure and non-wet phase pressure, respectively; σ_c is the surface tension, mN/m; P_c is the capillary pressure, MPa.

3.4. Vapor-Liquid Fugacity Equilibrium

Fugacity means the potential a molecule has to leave its original group. As for a stable system containing both a vapor phase and a liquid phase, it is natural to summarize that the condition for equilibrium is where the vapor-phase fugacity is equal to the liquid-phase fugacity. The mentioned basic equilibrium condition comes from the profound theory of molecular-phase behavior in a bulk situation. As discussed, although adsorption, shifted critical properties, and an enlarged capillary pressure varies nanoconfined phase behavior, the basic condition for fugacity equilibrium still holds. However, the concrete way to calculate fugacity changes when incorporating the above mechanisms in this work.

At first, the profound classic PR-EOS equation is provided, as per Equations (12)–(16). Notably, some research has modified the primary PR-EOS equation by, e.g., adding terms to describe surface-wall interactions. These modified PR-EOS equations are designed to incorporate the mentioned mechanisms (mainly the shifted critical properties) by using

the formula itself. In contrast, in this work, the mechanisms, including shifted critical properties, adsorption-phase thickness, and capillary pressure, are incorporated by utilizing a complete calculation procedure, as presented in Figure 2. Therefore, the original PR-EOS is employed here, and the above mechanisms are coupled in the calculation procedures.

$$P = \frac{RT}{V_m - b} - \frac{a}{V_m(V_m + b) + b(V_m - b)} \quad (12)$$

$$a = 0.45724 \frac{R^2 T_c^2}{P_c} \alpha \quad (13)$$

$$b = 0.0788 \frac{RT_c}{P_c} \quad (14)$$

$$\alpha = [1 + \kappa(1 - \sqrt{T/T_c})]^2 \quad (15)$$

$$\kappa = 0.37464 + 1.54226\omega - 0.26992\omega^2 \quad (16)$$

where P and T are the pressure and temperature, respectively; R is the universal gas constant, 8.314 J/mol/K; V_m is the molar volume, m³/mol; ω is the acentric factor, which is dimensionless.

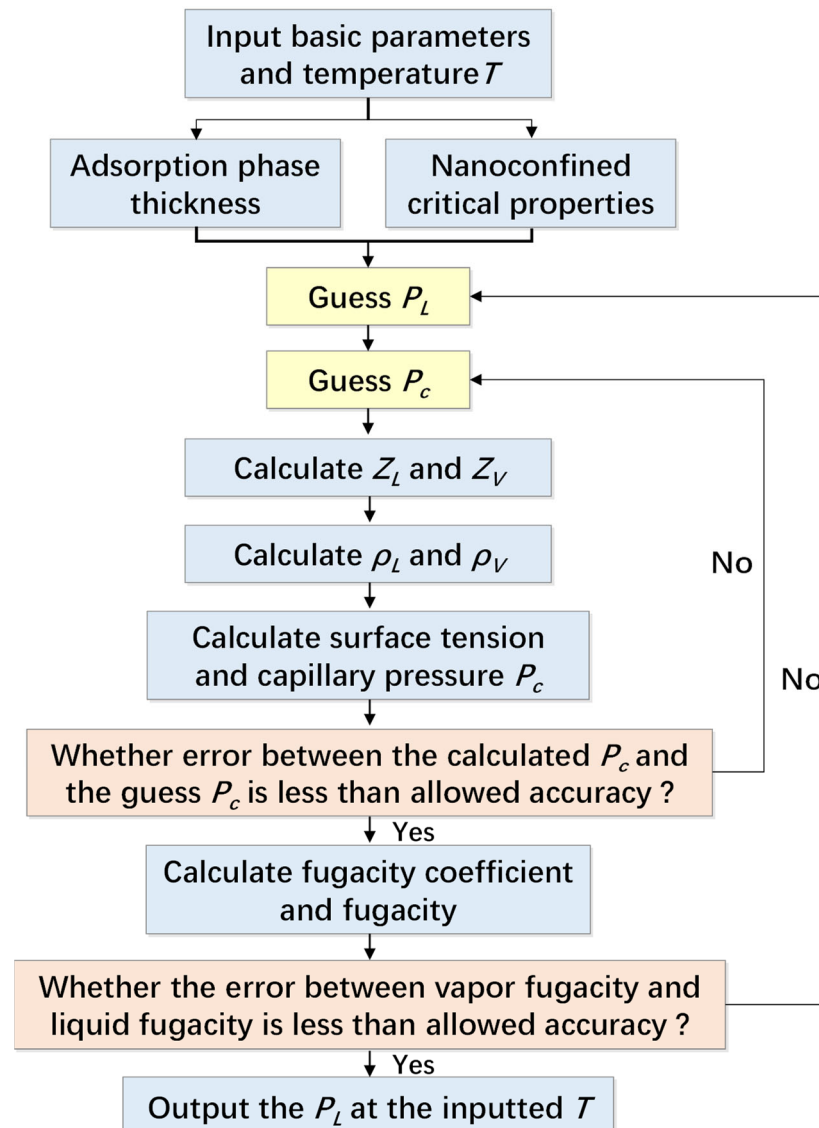


Figure 2. Calculation procedures for nanoconfined methane phase envelope.

It should be highlighted that the shifted critical properties (P_c , T_c) are used here, instead of P_{cb} and T_{cb} , to reproduce bulk-molecule-phase behavior. Equation (12) can be transformed into the following Equations (17) and (18) in terms of vapor-phase and liquid-phase compressibility. The inherent factor distinguishing Equations (17) and (18) is the capillary pressure; as a result, the basic parameters, such as A_L , B_L , A_V , and B_V , are obtained by using liquid-phase pressure (P_L) and vapor-phase pressure (P_V), respectively. The influence of capillary pressure on nanoconfined phase behavior is embodied here.

$$Z_L^3 - (1 - B_L)Z_L^2 + (A_L - 3B_L^2 - 2B_L)Z_L - (A_L B_L - B_L^2 - B_L^3) = 0 \quad (17)$$

$$Z_V^3 - (1 - B_V)Z_V^2 + (A_V - 3B_V^2 - 2B_V)Z_V - (A_V B_V - B_V^2 - B_V^3) = 0 \quad (18)$$

$$A_L = \frac{aP_L}{R^2T^2} \quad (19)$$

$$B_L = \frac{bP_L}{RT} \quad (20)$$

$$A_V = \frac{aP_V}{R^2T^2} \quad (21)$$

$$B_V = \frac{bP_V}{RT} \quad (22)$$

where Z_L and Z_V are liquid-phase and vapor-phase compressibility, respectively; P_L and P_V are liquid-phase pressure and vapor-phase pressure, respectively.

Furthermore, the molar density for the liquid phase (ρ_L) and vapor phase (ρ_V) can be obtained by using the following expressions.

$$\rho_L = \frac{P_L Z_L}{RT} \quad (23)$$

$$\rho_V = \frac{P_V Z_V}{RT} \quad (24)$$

Then, according to the Parachor model, the methane surface tension can be calculated based on the liquid-phase and vapor-phase molar densities. The Equation (25) is utilized to calculate capillary pressure.

$$\sigma_c = (p_a \rho_L - p_a \rho_V)^n \quad (25)$$

where P_a is the methane Parachor; n is an empirical coefficient, which is 4 in this work.

After that, the liquid-phase and vapor-phase fugacity coefficients have the following expressions, as presented by Equations (26) and (27); moreover, the liquid-phase and vapor-phase fugacity can be calculated, respectively, by multiplying the fugacity coefficient with pressure. The fugacity equilibrium is described by Equation (28).

$$\ln \phi^L = -\ln(Z_L - B_L) + (Z_L - 1) - \frac{A_L}{2\sqrt{2}B_L} \ln \frac{Z_L + (1 + \sqrt{2})B_L}{Z_L + (1 - \sqrt{2})B_L} \quad (26)$$

$$\ln \phi^V = -\ln(Z_V - B_V) + (Z_V - 1) - \frac{A_V}{2\sqrt{2}B_V} \ln \frac{Z_V + (1 + \sqrt{2})B_V}{Z_V + (1 - \sqrt{2})B_V} \quad (27)$$

$$\phi^L P_L = \phi^V P_V \quad (28)$$

where Φ_L and Φ_V are the liquid-phase and vapor-phase fugacity coefficients, respectively.

As depicted in Figure 2, the procedures to determine the methane phase envelope are provided in detail. There are two iterative calculations in the provided procedures. At first, P_L , the liquid-phase pressure at the inputted temperature, should be guessed. Then, in accordance with the calculation procedures, the liquid-phase and vapor-phase fugacity can be obtained, and their difference is calculated. The guessed P_L would be the right solution if the difference is less than the allowed accuracy; otherwise, a new P_L should be guessed,

and the calculation procedures executed again. At the same time, an iteration calculation on capillary pressure is performed as well. Similarly, capillary pressure as a function of the liquid-phase and vapor-phase molar densities cannot be accurately obtained at the initial point; therefore, a guessed P_c is utilized at first. Then, after calculating Z_V , Z_L , ρ_L , and ρ_V , capillary pressure can be calculated by using the Parachor model. Then, if the guessed P_c and the calculated P_c are a good match, then the capillary pressure is obtained; otherwise, one should give another guess for P_c and iterate the procedures. In short, the calculation procedures above consider the adsorption-phase thickness, shifted critical properties, and capillary pressure well, and the nanoconfined methane phase behavior can be presented.

4. Model Validation

In order to assess the reliability of the proposed model, three datasets for the methane phase diagram, which were obtained by using various approaches, including molecular simulation, the Lattice Boltzmann method, and modified EOS, are compiled. Given the intricacies involved in precisely characterizing nanoconfined methane phase behavior, leveraging results from multiple research approaches offers a comprehensive and relatively objective evaluation of the proposed model. In addition to considering the influence of pore size, the wettability effect closely linked to surface type is taken into account. For the simulation by Jin et al. (2017) [49], the surface type was graphite, exhibiting a certain affinity for methane. Therefore, a contact angle of 60° was inputted into the proposed model when reproducing the bulk methane phase behavior. The contact angle inputted to reproduce the results in Huang et al. (2020) [50] is 76° , which is consistent with the contact angle used in this work. Notably, Wang and Aryana (2020) [51] omitted consideration of capillary pressure; consequently, the inputted contact angle was set at 90° , resulting in zero capillary pressure in this case (see Table 1).

Table 1. Basic parameters collected to reproduce nanoconfined methane behavior.

| Contributions | Approach | Pore Size | Surface Type | Inputted Contact Angle |
|----------------------------|--------------------------|-----------|---|------------------------|
| Jin et al., 2017 [49] | Molecular simulation | Bulk | Graphite | 60° |
| Huang et al., 2020 [50] | Lattice Boltzmann Method | 10 nm | Contact angle is 76° , as reported | 76° |
| Wang and Aryana, 2021 [51] | Theoretical model | 5 nm | / | 90° |

In this section, the key parameter under comparison is the saturation vapor and liquid densities at different temperatures, as illustrated in Figure 3. At a specified temperature, two densities emerge in accordance with the saturation curve in Figure 3; the greater one represents the liquid-phase density, and the other is the vapor-phase density. Notably, the proposed model demonstrates excellent agreement with the results from previous research. However, a relatively large error is observed between the proposed model and that of Wang and Aryana (2021) [51]. This deviation may be attributed to the absence of consideration for adsorption-phase thickness in Wang and Aryana (2021) [51]. The adsorption-phase thickness narrows the pore size, further enhancing the magnitude of the shift in the critical properties. In summary, it can be asserted that the proposed model effectively reproduces the methane phase behavior in nanopores, as indicated by the current references. Additionally, based on Figure 3, the impact of pore size shrinkage on nanoconfined methane phase behavior is evident. The entire area covered by the phase envelope contracts, suggesting a decline in both saturated vapor and liquid phase densities with increasing nanoconfinement. It is crucial to highlight that the existing theoretical model, exemplified by the research of Wang and Aryana (2021) [51], falls short of fully coupling the mechanisms contributing to abnormal nanoconfined phase behavior. Therefore, this research is imperative for establishing the proposed model and

shedding light on the individual effects of each mechanism on the methane phase envelope in nanopores.

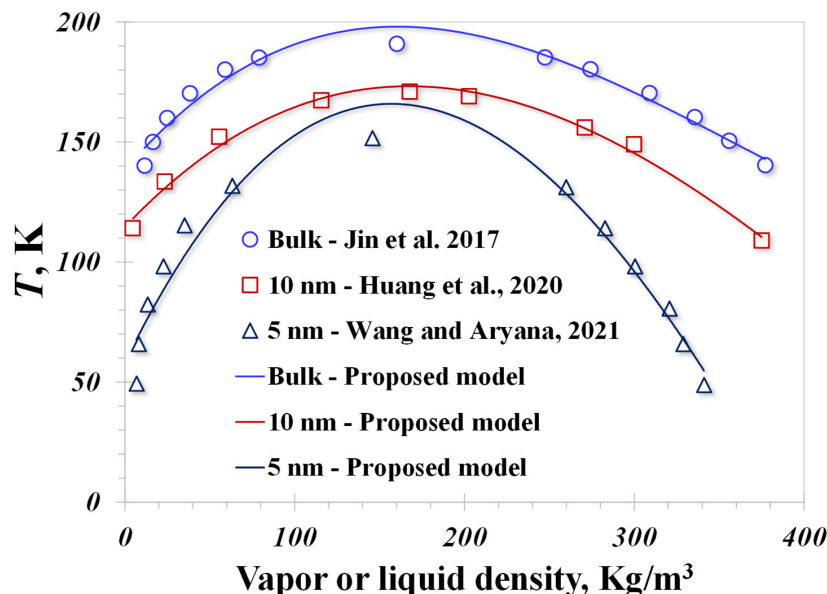


Figure 3. The proposed model versus previous contributions for saturation vapor-liquid densities.

5. Results and Discussion

The establishment of a fully coupled model to capture nanoconfined methane phase behavior is a groundbreaking achievement, and its reliability is thoroughly clarified. To date, primary research efforts have focused on the impact of pore size on nanoconfined phase behavior. However, a comprehensive sensitivity analysis is still lacking. Particularly, the role of capillary pressure, representing the substantial difference between vapor-phase pressure and liquid-phase pressure, on the methane phase diagram in nanopores remains unclear. Additionally, the wettability effect, arising from robust molecule-wall interactions in nanopores, amplifies the shift in the magnitude of the critical properties and capillary pressure. Hence, at this juncture, it is significantly necessary to utilize the proposed model to shed light on the aforementioned unsolved issues.

5.1. Pore Size

Five sets of pore sizes were employed to illustrate the impact of pore size on the nanoconfined methane phase diagram. The contact angle is fixed at 60° . As depicted in Figure 4, the phase diagram exhibits a surprising variation with shrinkage in pore size. Under a stronger nanoconfinement effect, the phase diagram curve becomes more vertical. Additionally, based on observations, the variation pattern is distinguished by a temperature threshold of 168 K. When the temperature is below 168 K, the phase diagram decreases with decreasing nanopore size. Conversely, as the temperature surpasses 168 K, the phase diagram increases with a smaller pore size. In other words, the methane molecules that exist in the vapor phase in large nanopores turn into the liquid phase in smaller nanopores when the temperature is below 168 K. This process simultaneously reverses completely when the temperature exceeds 168 K, with the liquid-phase methane molecules in large nanopores transitioning into the vapor phase in small nanopores. It is crucial to explore the underlying mechanism behind this phenomenon. Due to the presence of capillary pressure, the vapor-phase pressure in nanopores is significantly higher than the liquid-phase pressure, which is in contrast to the macropore condition, where the vapor-phase pressure equals the liquid-phase pressure. This relatively high pressure enhances the potential for the vapor phase to transition into the liquid phase, aligning with Kelvin's theory that the presence of the meniscus contributes to liquidation. Regarding the phenomenon at relatively high temperatures, the attributed factor may be the shifted critical

properties, a unique variation confirmed by experimental observations and molecular results. As a result, there exists a specific temperature threshold that divides the impact of pore size on the nanoconfined methane phase diagram. The existing phase of methane in nanopores differs from that evaluated by the conventional phase diagram. Additionally, the phase diagram at temperatures below the specific threshold is governed by capillary pressure, while at higher temperatures, it is dominated by shifted critical properties.

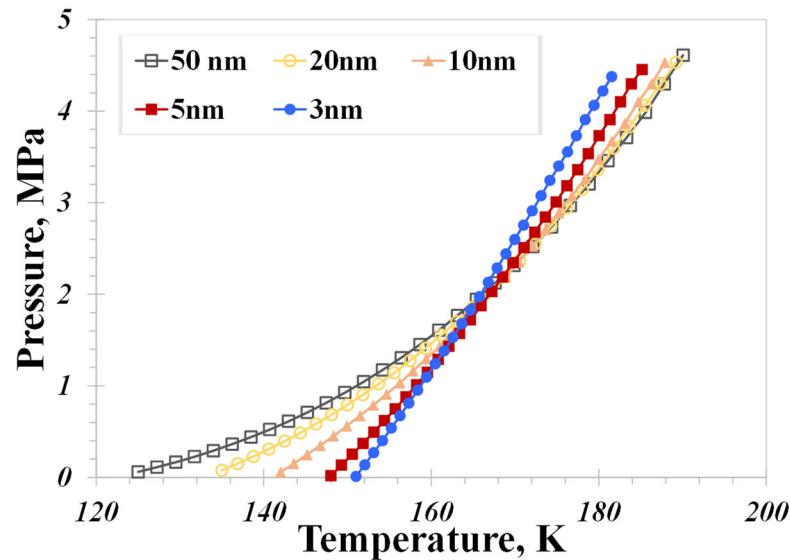


Figure 4. Nanoconfined methane phase diagram versus nanopore size.

The coexistence curve with different pore sizes is depicted in Figure 5, where the hollow marks represent the vapor density, and the solid marks represent the liquid density. Evidently, the area covered by the curve shrinks with the decrease in pore size, signifying an increase in the saturated vapor-phase density and a reduction in the saturated liquid-phase density. The presence of capillary pressure, which enhances vapor pressure with pore size shrinkage, is responsible for the increase in vapor density. Additionally, in accordance with the formula for liquid density (Equation (23)), the decline in liquid-phase density should be attributed to the variation in liquid-phase compressibility, which is a function of nanoconfined critical properties.

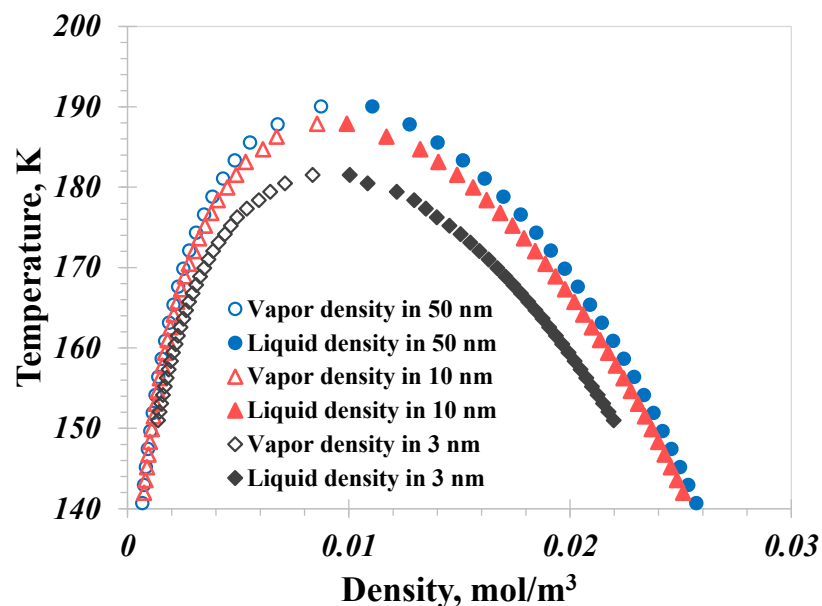


Figure 5. Methane vapor-liquid coexistence curve with different nanopore sizes.

5.2. Surface Wettability

As discussed, the wettability effect, which is inherently linked to the molecule-surface interaction strength, plays a critically significant role in influencing fluid behavior in nanopores. However, little research has been conducted to investigate the wettability effect on nanoconfined phase behavior. Moreover, the wettability effect heavily depends on the distance the molecule is from the solid phase. Therefore, two sets of pore sizes are used here, and the surface contact angle ranges from 30° to 150° . In order to quantify the phase diagram effectively, the T_{min} and T_{max} , representing the temperatures corresponding to the maximum and minimum pressures on the methane phase diagram, respectively, are utilized here. As presented in Figure 6, for the 50 nm pore size, the phase diagram becomes more vertical with decreasing contact angle. In detail, the vapor-phase molecules in nanopores with a large contact angle may transition to the liquid phase in nanopores with a small contact angle. This suggests that intensifying molecule-surface interaction would enhance the molecular potential to change to the liquid phase. As illustrated in Figure 6B, the variation caused by surface wettability is obvious, with the T_{min} value declining rapidly with increasing surface contact angle. It means the discrepancy in the existence phase becomes more evident at relatively low pressure. From Figure 6A, the phase diagrams at high-pressure conditions almost coincide, indicating that the wettability effect is negligible when the pressure is higher than 2 MPa.

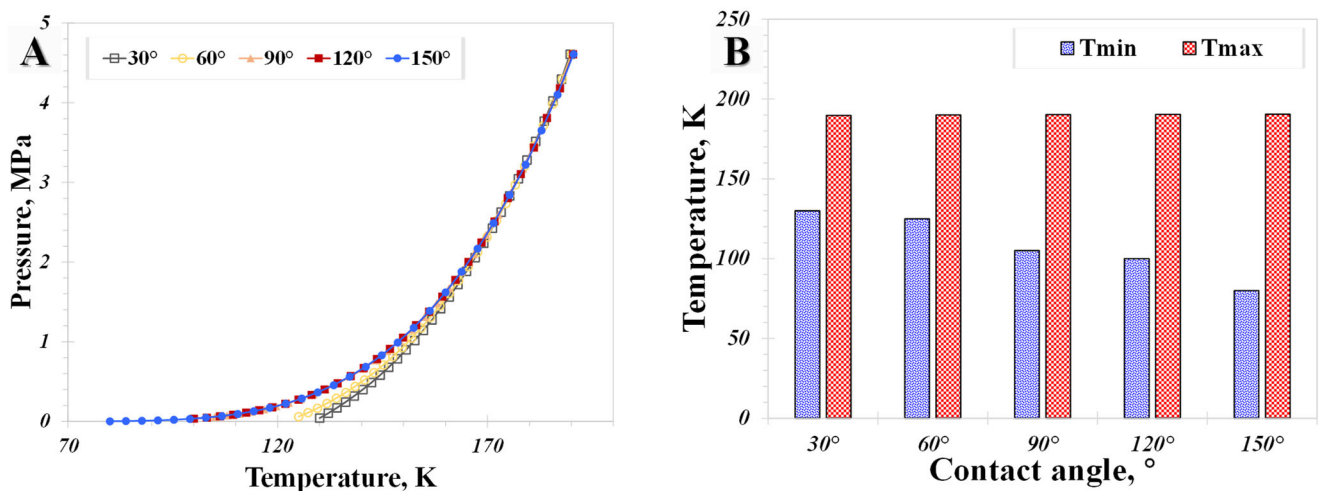


Figure 6. Wettability versus methane phase diagram with a pore size of 50 nm.

When pore size becomes 5 nm, the methane phase diagram when the contact angle is less than 60° is significantly different. It can be demonstrated that the influence of the wettability effect on nanoconfined phase behavior becomes more evident when the pore size is less than 5 nm. As a result, the utmost caution should be paid to take care of the wettability effect in nanopores, particularly in cases where the nanopore size is less than 5 nm. As presented in Figure 7B, the T_{min} could decline by as much as 87.3% when the contact angle changes from 30° to 150° . Moreover, it can be observed in Figure 7A that there is a relatively large fall in terms of the T_{min} value with a contact angle that spans from 60° to 90° . It indicates that the phase diagram changes considerably when the contact angle ranges from 60° to 90° , and the existence phase of methane is complex in this range. As a result, for smaller nanopores, 90° is a critical value for distinguishing the nanoconfined phase behavior. Basically, the phase diagram is almost unchanged when the contact angle is larger than 90° , and a dramatic change happens when the contact angle becomes less than 90° .

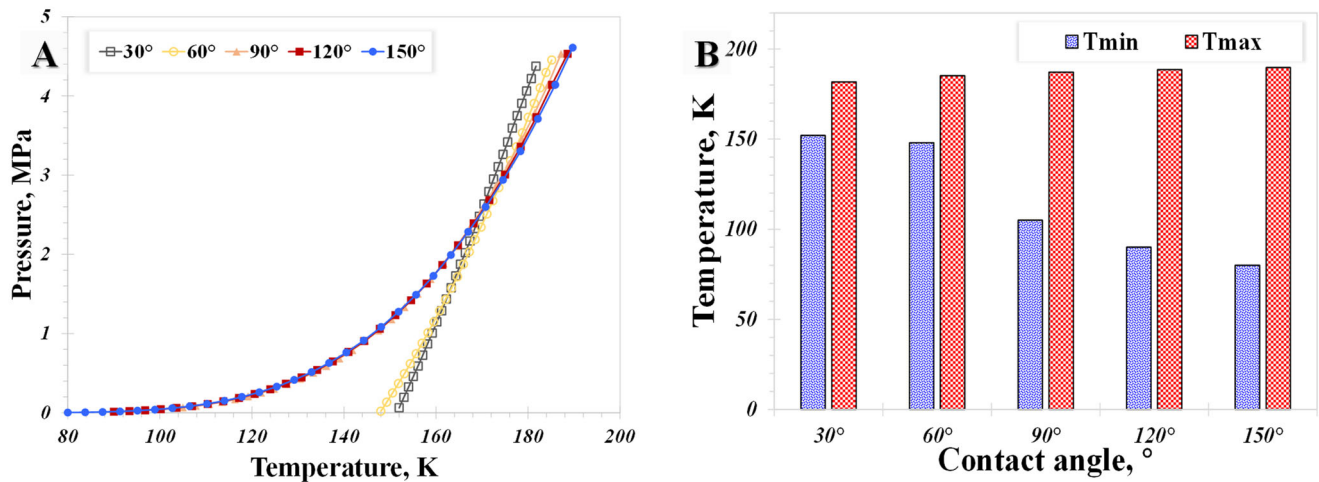


Figure 7. Wettability versus methane phase diagram when the pore size is 5 nm.

5.3. Capillary Pressure

Capillary pressure, representing the pressure difference between vapor-phase pressure and liquid-phase pressure, requires more attention when it comes to the nanoscale. In this section, the pore size was set as 5 nm, and two sets of contact angles were utilized: 60° for typical, strong surface-molecule interaction strength and 120° for the weak version. Evidently, it can be observed from Figure 8 that the influence of capillary pressure on the nanoconfined methane phase diagram is considerable. The surface contact angle is 60°. As introduced above, the T_{min} value is nearly 80 K in the case of neglecting capillary pressure, whereas the value varies at 149 K once the capillary pressure is considered. Therefore, the capillary pressure is the main factor leading to the phenomenon where the phase diagram curve becomes vertical. Additionally, in Figure 8B, it can be observed that the liquid-phase density, when considering capillary pressure, would be slightly less than when neglecting capillary pressure, and the vapor-phase density is almost irrelevant regarding capillary pressure.

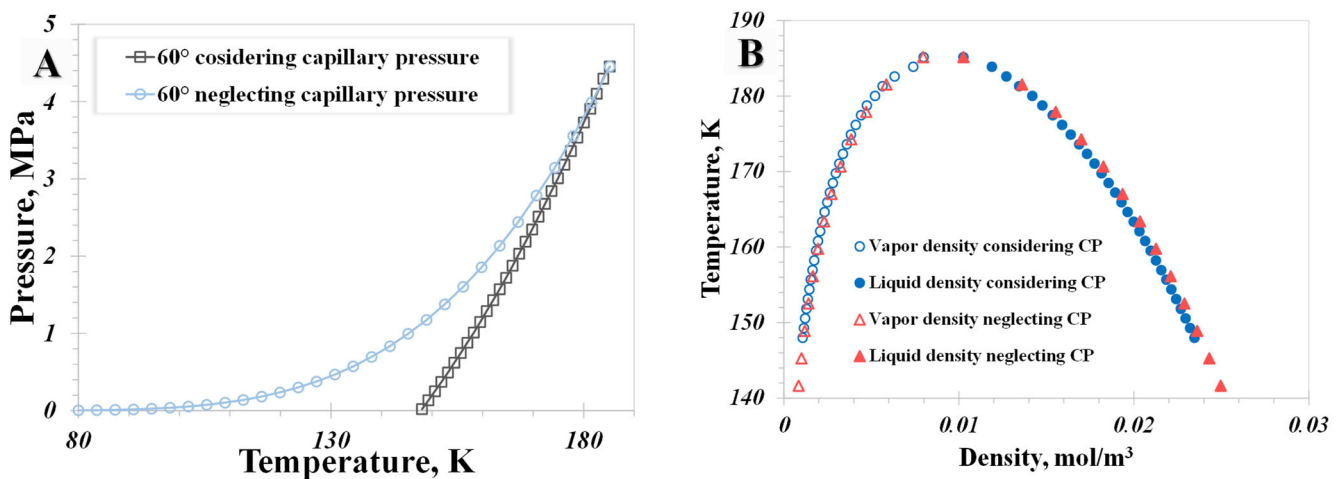


Figure 8. Impact of capillary pressure on methane phase diagram when the contact angle is 60°.

Subsequently, the surface contact angle was set at 120° to identify the effect of capillary pressure on methane phase behavior with weak molecule-surface interactions. As presented in Figure 9A,B, the phase diagrams almost coincide, indicating that capillary pressure has little influence on varying the phase diagram. In contrast with the performance in Figure 8A,B, it can be summarized that the impact of capillary pressure is heavily dependent on the surface contact angle. The capillary pressure cannot be neglected until

the contact angle is less than 90° . Similarly, vapor-liquid coexistence performance is further investigated in Figure 9B, where both the vapor- and liquid-phase densities change little when considering or neglecting the capillary pressure.

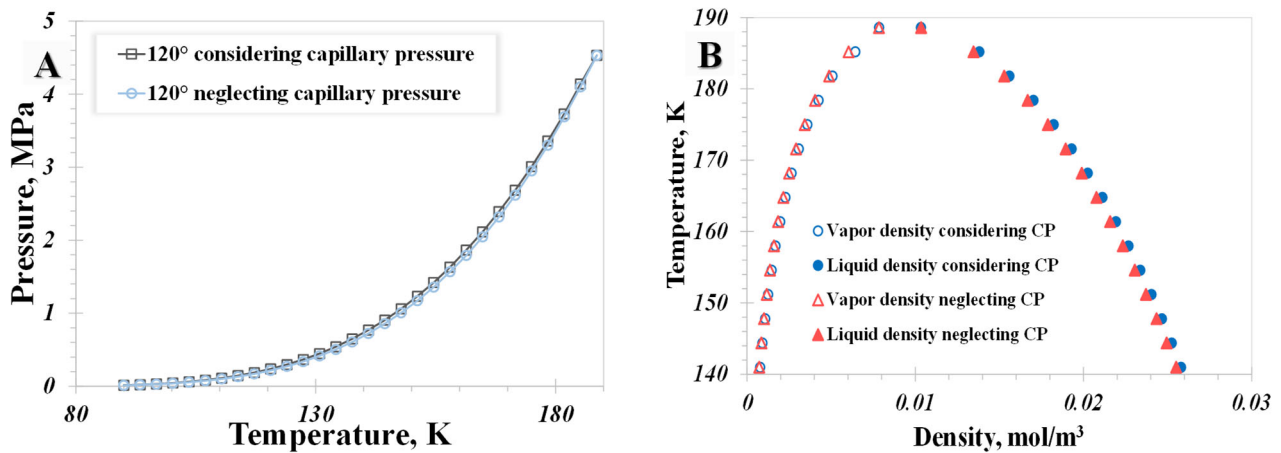


Figure 9. Impact of capillary pressure on methane phase diagram when the contact angle is 120° .

5.4. Shifted Critical Properties

Shifted critical properties are a well-acknowledged phenomenon for nanoconfined methane, primarily controlled by pore size. In this case, two sets of pore sizes were used. As presented in Figure 10A,B, the discrepancy induced by a shift in the critical properties is quite evident. At a specific pressure, the error in the corresponding temperatures on the phase diagram curves could reach as high as 7.1%. In contrast, when the pore size was enlarged to 50 nm, the methane diagram that considers the shifted critical properties is almost the same as that neglecting the shift. It can be demonstrated that the impact of shifted critical properties could reasonably be overlooked for a large pore size.

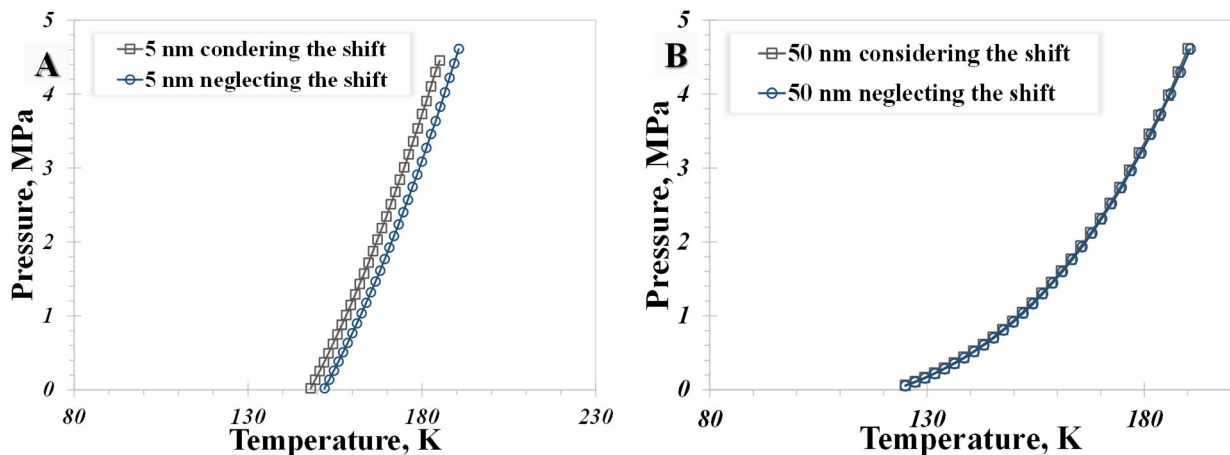


Figure 10. Impact of shifted critical properties on nanoconfined methane phase diagram.

6. Conclusions

1. Based on the fundamental vapor-liquid fugacity equilibrium, we established a fully coupled model to explore the methane phase diagram in nanopores. This model simultaneously considers adsorption-phase thickness, capillary pressure, and shifted critical properties. The reliability of the model in reproducing nanoconfined methane phase diagrams was thoroughly clarified by comparing it against experimental data and MD results, utilizing different methods and surface types.
2. A distinctive temperature, 168 K in our calculation case, serves as a dividing point for the impact of pore size on the nanoconfined methane phase diagram. Below 168 K,

methane molecules in a vapor phase in large nanopores transition to the liquid phase in smaller nanopores. The presence of capillary pressure, which enhances vapor-phase pressure as pore size decreases, is responsible for the increase in vapor density.

3. The influence of the wettability effect on nanoconfined phase behavior becomes more pronounced when the pore size is less than 5 nm. The methane phase diagram remains almost unchanged when the contact angle is larger than 90°, with a dramatic change occurring when the contact angle is less than 90°. Capillary pressure emerges as the main factor causing the phase diagram curve to become vertical. The impact of shifted critical properties might reasonably be overlooked when the pore size exceeds 50 nm.

Author Contributions: Validation, J.L.; Formal analysis, L.C.; Investigation, C.Z.; Resources, Z.C.; Data curation, R.Z.; Writing—original draft, G.W.; Writing—review & editing, Y.P.; Supervision, Z.S. All authors have read and agreed to the published version of the manuscript.

Funding: This research was funded by the Open Fund of State Key Laboratory of Shale Gas Exploration (KLSGE202104), and the Natural Science Foundation Projects of Chongqing City (cstc2021jcyj-msxmX0453) supported part of this work. The first author also acknowledges the National Natural Science Foundation Projects of China (No. 52104099, No. 52104021, and No. 51974328) and the Natural Science Foundation Projects of Jiangsu Province (No. BK20210508).

Data Availability Statement: Data are contained within the article.

Conflicts of Interest: The authors declare no conflicts of interest.

References

1. York, R.; Bell, S.E. Energy transitions or additions: Why a transition from fossil fuels requires more than the growth of renewable energy. *Energy Res. Soc. Sci.* **2019**, *51*, 40–43. [[CrossRef](#)]
2. Liu, F.; Mauzerall, D.L.; Zhao, F.; Hao, H. Deployment of fuel cell vehicles in China: Greenhouse gas emission reductions from converting the heavy-duty truck fleet from diesel and natural gas to hydrogen. *Int. J. Hydrog. Energy* **2021**, *46*, 17982–17997. [[CrossRef](#)]
3. Shamlooh, M.; Hussein, I.A.; Nasser, M.S.; Magzoub, M.; Salehi, S. Development of pH-controlled aluminum-based polymeric gel for conformance control in sour gas reservoirs. *ACS Omega* **2020**, *5*, 24504–24512. [[CrossRef](#)] [[PubMed](#)]
4. Suboyin, A.; Rahman, M.M.; Haroun, M. Hydraulic fracturing design considerations, water management challenges and insights for Middle Eastern shale gas reservoirs. *Energy Rep.* **2020**, *6*, 745–760. [[CrossRef](#)]
5. Yu, P.; Dempsey, D.; Archer, R. Techno-Economic feasibility of enhanced geothermal systems (EGS) with partially bridging Multi-Stage fractures for district heating applications. *Energy Convers. Manag.* **2022**, *257*, 115405. [[CrossRef](#)]
6. Soleymanzadeh, A.; Helalizadeh, A.; Jamialahmadi, M.; Soulgani, B.S. Development of a new model for prediction of cementation factor in tight gas sandstones based on electrical rock typing. *J. Nat. Gas Sci. Eng.* **2021**, *94*, 104128. [[CrossRef](#)]
7. Knapp, L.J.; Ardakani, O.H.; Uchida, S.; Nanjo, T.; Otomo, C.; Hattori, T. The influence of rigid matrix minerals on organic porosity and pore size in shale reservoirs: Upper Devonian Duvernay Formation, Alberta, Canada. *Int. J. Coal Geol.* **2020**, *227*, 103525.
8. Pang, Y.; Wang, S.; Yao, X.; Hu, X.; Chen, S. Evaluation of gas adsorption in nanoporous shale by simplified local density model integrated with pore structure and pore size distribution. *Langmuir* **2022**, *38*, 3641–3655. [[CrossRef](#)]
9. Sun, Z.; Huang, B.; Yan, S.; Wang, S.; Wu, K.; Yu, W.; Li, Y.; Wang, S. Nanoconfined Methane Thermodynamic Behavior below Critical Temperature: Liquid–Vapor Coexistence Curve under Wettability Effect. *Ind. Eng. Chem. Res.* **2022**, *61*, 4971–4979.
10. Mohagheghian, E.; Hassanzadeh, H.; Chen, Z. Evaluation of shale-gas-phase behavior under nanoconfinement in multimechanistic flow. *Ind. Eng. Chem. Res.* **2020**, *59*, 15048–15057. [[CrossRef](#)]
11. Jia, B.; Xian, C.; Tsau, J.S.; Zuo, X.; Jia, W. Status and outlook of oil field chemistry-assisted analysis during the energy transition period. *Energy Fuels* **2022**, *36*, 12917–12945. [[CrossRef](#)]
12. Jia, B.; Xian, C.G. Permeability measurement of the fracture-matrix system with 3D embedded discrete fracture model. *Pet. Sci.* **2022**, *19*, 1757–1765. [[CrossRef](#)]
13. Wang, T.; Tian, S.; Li, G.; Zhang, L.; Sheng, M.; Ren, W. Molecular simulation of gas adsorption in shale nanopores: A critical review. *Renew. Sustain. Energy Rev.* **2021**, *149*, 111391. [[CrossRef](#)]
14. Rabani, R.; Merabia, S.; Pishavar, A. Conductive heat transfer through nanoconfined argon gas: From continuum to free-molecular regime. *Int. J. Therm. Sci.* **2023**, *192*, 108391. [[CrossRef](#)]
15. Sun, Z.; Li, X.; Liu, W.; Zhang, T.; He, M.; Nasrabadi, H. Molecular Dynamics of Methane Flow Behavior through Realistic Organic Nanopores under Geologic Shale Condition: Pore size and Kerogen Types. *Chem. Eng. J.* **2020**, *398*, 124341.
16. Zhang, T.; Javadpour, F.; Li, J.; Zhao, Y.; Zhang, L.; Li, X. Pore-scale perspective of gas/water two-phase flow in shale. *SPE J.* **2021**, *26*, 828–846. [[CrossRef](#)]

17. Zuo, H.; Zhai, C.; Deng, S.; Jiang, X.; Javadpour, F. Lattice Boltzmann modeling of gaseous microflow in shale nanoporous media. *Fuel* **2023**, *337*, 127087. [[CrossRef](#)]
18. Le, T.H.H.; Morita, A.; Tanaka, T. Refractive index of nanoconfined water reveals its anomalous physical properties. *Nanoscale Horiz.* **2020**, *5*, 1016–1024. [[CrossRef](#)]
19. Barisik, M.; Beskok, A. Scale effects in gas nano flows. *Phys. Fluids* **2014**, *26*, 052003. [[CrossRef](#)]
20. Bardhan, R.; Hedges, L.O.; Pint, C.L.; Javey, A.; Whitlam, S.; Urban, J.J. Uncovering the intrinsic size dependence of hydrating phase transformations in nanocrystals. *Nat. Mater.* **2013**, *12*, 905–912. [[CrossRef](#)]
21. Duan, X.; Hu, Z.; Shao, N.; Li, W.; Li, Y.; Chang, J.; Shen, R. Establishment of a new slip permeability model of gas flow in shale nanopores based on experimental and molecular dynamics simulations studies. *J. Pet. Sci. Eng.* **2020**, *193*, 107365. [[CrossRef](#)]
22. Wu, K.; Chen, Z.; Li, X.; Guo, C.; Wei, M. A model for multiple transport mechanisms through nanopores of shale gas reservoirs with real gas effect–adsorption-mechanic coupling. *Int. J. Heat Mass Transf.* **2016**, *93*, 408–426.
23. Song, W.; Yao, J.; Wang, D.; Li, Y.; Sun, H.; Yang, Y. Dynamic pore network modelling of real gas transport in shale nanopore structure. *J. Pet. Sci. Eng.* **2020**, *184*, 106506. [[CrossRef](#)]
24. Xu, J.; Wu, K.; Li, Z.; Pan, Y.; Li, R.; Li, J.; Chen, Z. A model for gas transport in dual-porosity shale rocks with fractal structures. *Ind. Eng. Chem. Res.* **2018**, *57*, 6530–6537.
25. Shen, W.; Song, F.; Hu, X.; Zhu, G.; Zhu, W. Experimental study on flow characteristics of gas transport in micro-and nanoscale pores. *Sci. Rep.* **2019**, *9*, 10196. [[CrossRef](#)] [[PubMed](#)]
26. Roy, S.; Raju, R.; Chuang, H.F.; Cruden, B.A.; Meyyappan, M. Modeling gas flow through microchannels and nanopores. *J. Appl. Phys.* **2003**, *93*, 4870–4879.
27. Sheng, G.L.; Zhao, H.; Su, Y.L.; Javadpour, F.; Wang, C.; Zhou, Y.; Liu, J.; Wang, H. An analytical model to couple gas storage and transport capacity in organic matter with noncircular pores. *Fuel* **2020**, *268*, 117288. [[CrossRef](#)]
28. Pang, Y.; Hu, X.; Wang, S.; Chen, S.; Soliman, M.Y.; Deng, H. Characterization of adsorption isotherm and density profile in cylindrical nanopores: Modeling and measurement. *Chem. Eng. J.* **2020**, *396*, 125212.
29. Huang, L.; Zhou, W.; Xu, H.; Wang, L.; Zou, J.; Zhou, Q. Dynamic fluid states in organic-inorganic nanocomposite: Implications for shale gas recovery and CO₂ sequestration. *Chem. Eng. J.* **2021**, *411*, 128423. [[CrossRef](#)]
30. Liu, J.; Zhang, T.; Sun, S. Mechanism Analysis of Shale Gas Adsorption under Carbon Dioxide–Moisture Conditions: A Molecular Dynamic Study. *Energy Fuels* **2022**, *36*, 14865–14873.
31. Zhao, W.; Jia, C.; Zhang, T.; Jiang, L.; Li, X.; Jiang, Z.; Zhang, F. Effects of nanopore geometry on confined water flow: A view of lattice Boltzmann simulation. *Chem. Eng. Sci.* **2021**, *230*, 116183. [[CrossRef](#)]
32. Fathi, E.; Akkutlu, I.Y. Lattice Boltzmann method for simulation of shale gas transport in kerogen. *SPE J.* **2013**, *18*, 27–37. [[CrossRef](#)]
33. Li, J.; Wu, K.; Chen, Z.; Wang, K.; Luo, J.; Xu, J.; Li, R.; Yu, R.; Li, X. On the negative excess isotherms for methane adsorption at high pressure: Modeling and experiment. *SPE J.* **2019**, *24*, 2504–2525. [[CrossRef](#)]
34. Garberoglio, G.; Skoulidas, A.I.; Johnson, J.K. Adsorption of gases in metal organic materials: Comparison of simulations and experiments. *J. Phys. Chem. B* **2005**, *109*, 13094–13103. [[CrossRef](#)] [[PubMed](#)]
35. Song, Z.; Song, Y.; Guo, J.; Zhang, Z.; Hou, J. Adsorption induced critical shifts of confined fluids in shale nanopores. *Chem. Eng. J.* **2020**, *385*, 123837.
36. Islam, A.W.; Patzek, T.W.; Sun, A.Y. Thermodynamics phase changes of nanopore fluids. *J. Nat. Gas Sci. Eng.* **2015**, *25*, 134–139. [[CrossRef](#)]
37. Sedghi, M.; Piri, M. Capillary condensation and capillary pressure of methane in carbon nanopores: Molecular Dynamics simulations of nanoconfinement effects. *Fluid Phase Equilibria* **2018**, *459*, 196–207. [[CrossRef](#)]
38. Yu, P.; Dempsey, D.; Archer, R. A three-dimensional coupled thermo-hydro-mechanical numerical model with partially bridging multi-stage contact fractures in horizontal-well enhanced geothermal system. *Int. J. Rock Mech. Min. Sci.* **2021**, *143*, 104787. [[CrossRef](#)]
39. Sun, Z.; Huang, B.; Wang, S.; Wu, K.; Li, H.; Wu, Y. Hydrogen adsorption in nanopores: Molecule-wall interaction mechanism. *Int. J. Hydrog. Energy* **2023**, *48*, 33496–33508.
40. Cao, M.; Hirose, S.; Sharma, M.M. Factors controlling the formation of complex fracture networks in naturally fractured geothermal reservoirs. *J. Pet. Sci. Eng.* **2022**, *208*, 109642. [[CrossRef](#)]
41. Maurer, R.J.; Ruiz, V.G.; Camarillo-Cisneros, J.; Liu, W.; Ferri, N.; Reuter, K.; Tkatchenko, A. Adsorption structures and energetics of molecules on metal surfaces: Bridging experiment and theory. *Prog. Surf. Sci.* **2016**, *91*, 72–100. [[CrossRef](#)]
42. Wu, S.; He, Y.; Wang, J. Molecular Resolution Imaging of Adsorption of Dodecane on a Lignite Surface by Frequency Modulation AFM. *Energy Fuels* **2022**, *36*, 11861–11872. [[CrossRef](#)]
43. Zhang, K.; Jia, N.; Liu, L. CO₂ storage in fractured nanopores underground: Phase behaviour study. *Appl. Energy* **2019**, *238*, 911–928.
44. Humand, M.; Khorsand Movaghar, M.R. Critical temperature shift modeling of confined fluids using pore-size-dependent energy parameter of potential function. *Sci. Rep.* **2023**, *13*, 4842. [[CrossRef](#)]
45. Zarragoicoechea, G.J.; Kuz, V.A. Critical shift of a confined fluid in a nanopore. *Fluid Phase Equilibria* **2004**, *220*, 7–9. [[CrossRef](#)]
46. Feng, D.; Bakhshian, S.; Wu, K.; Song, Z.; Ren, B.; Li, J.; Hosseini, S.A.; Li, X. Wettability effects on phase behavior and interfacial tension in shale nanopores. *Fuel* **2021**, *290*, 119983.

47. Shen, A.; Liu, Y.; Ali, S.F. A model of spontaneous flow driven by capillary pressure in nanoporous media. *Capillarity* **2020**, *3*, 1–7.
48. Song, Y.; Song, Z.; Guo, J.; Feng, D.; Chang, X. Phase behavior and miscibility of CO₂–hydrocarbon mixtures in shale nanopores. *Ind. Eng. Chem. Res.* **2021**, *60*, 5300–5309.
49. Jin, B.; Bi, R.; Nasrabadi, H. Molecular simulation of the pore size distribution effect on phase behavior of methane confined in nanopores. *Fluid Phase Equilibria* **2017**, *452*, 94–102.
50. Huang, J.; Yin, X.; Barrufet, M.; Killough, J. Lattice Boltzmann simulation of phase equilibrium of methane in nanopores under effects of adsorption. *Chem. Eng. J.* **2021**, *419*, 129625. [[CrossRef](#)]
51. Wang, Y.; Aryana, S.A. Coupled confined phase behavior and transport of methane in slit nanopores. *Chem. Eng. J.* **2021**, *404*, 126502.

Disclaimer/Publisher’s Note: The statements, opinions and data contained in all publications are solely those of the individual author(s) and contributor(s) and not of MDPI and/or the editor(s). MDPI and/or the editor(s) disclaim responsibility for any injury to people or property resulting from any ideas, methods, instructions or products referred to in the content.